Efficient and Accurate Analysis of Large Metamaterial Structures with the Multilevel Fast Multipole Algorithm†

Özgür Ergül[1], Alper Ünal[1], and Levent Gürel[1,2]

[1]Department of Electrical and Electronics Engineering
[2]Computational Electromagnetics Research Center (BiLCEM)
Bilkent University, TR-06800, Bilkent, Ankara, Turkey
E-mail: ergul@ee.bilkent.edu.tr, runal@ug.bilkent.edu.tr, lgurel@bilkent.edu.tr

Abstract
Efficient and accurate solutions of electromagnetic problems related to large metamaterial (MM) structures are reported. The simulations of MMs are performed by formulating the electromagnetic interactions with the electric-field integral equation and solving the resulting dense matrix equation iteratively using multilevel fast multipole algorithm. Single and multiple layers of arrays of split ring resonators (SRRs) and thin wires (TWs) are investigated in detail. Combined metamaterials including both SRR and TW arrays are also considered to obtain double-negative medium.

1. Introduction

Metamaterials (MMs) are usually constructed by periodical arrangements of unit cells such as split ring resonators (SRRs) and thin wires (TWs). When these two types of cells are included in a single medium, composite metamaterials (CMMs) are obtained. CMMs present unusual electromagnetic properties due to the negative effective permittivity and permeability stimulated in the medium. In this paper, we specifically investigate the MM structures consisting of SRR and/or TW arrays, as depicted in Fig. 1. We carefully analyze these structures by taking into account that they actually have finite extent and exhibit interface properties. Without using the symmetry and periodicity of these structures, we accurately model large numbers of unit cells to understand their transmission properties. The surfaces are modelled by perfectly conducting sheets and the scattering problems are formulated by the electric-field integral equation (EFIE). With the triangulation of the conducting surfaces and employing Rao-Wilton-Glisson (RWG) [1] basis functions to expand the unknown surface current density, the resulting dense matrix equation is solved iteratively with the accelerated matrix-vector products by the multilevel fast multipole algorithm (MLFMA) [2]. We also utilize parallel computing techniques to increase our computational resources.

In this work, dimensions of the SRRs are in the order of microns to obtain negative effective permeability around 100 GHz [3]. The SRR array depicted in Fig. 1(a) is constructed by the arrangement of 11×18 SRRs. Around the resonance frequency, the transmission through the array is expected to decrease significantly due to the negative effective permeability introduced in the medium. Dimensions of the unit cells of the TW array depicted in Fig. 1(b)

†This work was supported by the Scientific and Technical Research Council of Turkey (TUBITAK) under Research Grant 105E172, by the Turkish Academy of Sciences in the framework of the Young Scientist Award Program (LG/TUBA-GEBIP/2002-1-12), and by contracts from ASELSAN and SSM

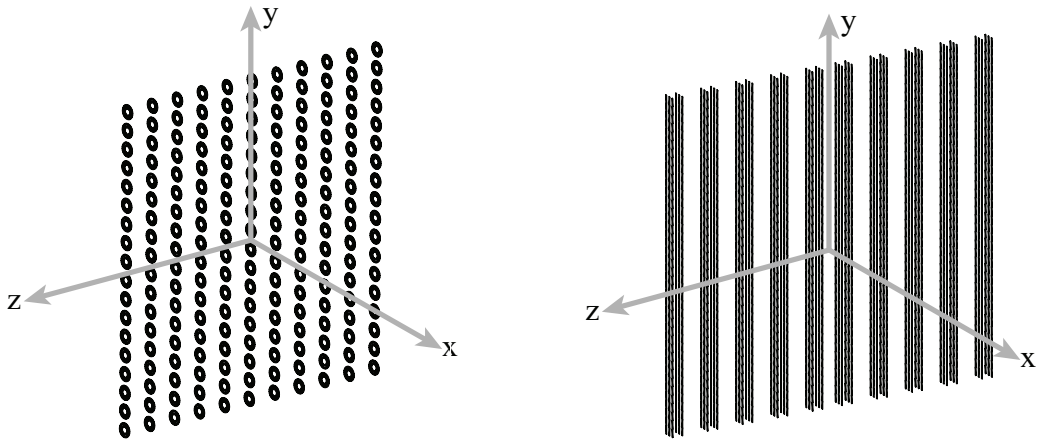

Fig. 1. (a) Single-layer SRR array obtained by the arrangement of 11×18 SRRs. (b) TW array having the same dimensions as the SRR array in Fig. 1(a).

are compatible with the dimensions of the SRRs and the array exhibits negative effective permittivity in a wide range of frequencies including 100 GHz. As a result, CMM structures obtained by the combination of the SRR and TW arrays in Fig. 1 are expected to show double-negative property around 100 GHz. In this paper, examples on 1-layer and 2-layer structures are provided to confirm the theoretical findings on practical cases.

2. MLFMA Solutions of Scattering Problems Involving Metamaterials

Both the SRR and TW geometries are modelled by open surfaces with zero thickness. Therefore, the scattering problems related to MMs are formulated by EFIE, which is applicable to open geometries. We solve the problems in frequency domain using phasor notation with the e^{-iwt} convention. First, the unknown current induced on the conducting surfaces is expanded in a series of basis functions $\boldsymbol{b}_n$, i.e.,

$$\boldsymbol{J}(\boldsymbol{r}) = \sum_{n=1}^{N} a_n \boldsymbol{b}_n(\boldsymbol{r}), \tag{1}$$

where a_n represents the unknown coefficients for $n = 1, 2, ..., N$ and N is the number of unknowns. Then, the application of moment methods leads to $N \times N$ dense matrix equation

$$\sum_{n=1}^{N} Z_{mn}^{E} a_n = v_m^{E}, \qquad m = 1, ..., N, \tag{2}$$

where

$$Z_{mn}^{E} = \int_{S_m} d\boldsymbol{r} \boldsymbol{t}_m(\boldsymbol{r}) \cdot \int_{S_n} d\boldsymbol{r'} \Big(\bar{\mathbf{I}} - \frac{\nabla\nabla'}{k^2} \Big) g(\boldsymbol{r}, \boldsymbol{r'}) \cdot \boldsymbol{b}_n(\boldsymbol{r'}) \tag{3}$$

represents the matrix element, and

$$v_m^{E} = \frac{i}{k\eta} \int_{S_m} d\boldsymbol{r} \boldsymbol{t}_m(\boldsymbol{r}) \cdot \boldsymbol{E^i}(\boldsymbol{r}) \tag{4}$$

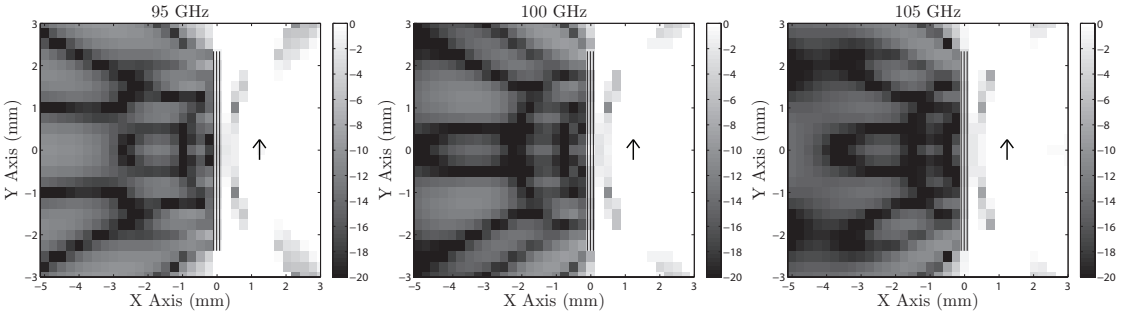

Fig. 2. Power transmission for the 1-layer TW array depicted in Fig. 1(a) at 95 GHz, 100 GHz, and 105 GHz. TWs and the ideal (Hertzian) dipole are also depicted in the figures and the transmission region is on the left of the array.

represents the mth element of the excitation vector. We apply the Galerkin scheme by choosing the testing functions $\boldsymbol{t}_m$ also as RWG. In (3) and (4), S_m and S_n symbolize the spatial supports of the mth testing and nth basis functions, respectively. In addition, k and η are the wavenumber and wave impedance associated with the host medium, and

$$g(\boldsymbol{r},\boldsymbol{r'}) = \frac{\exp(ikR)}{4\pi R} \qquad \Big(R = |\boldsymbol{r}-\boldsymbol{r'}|\Big) \tag{5}$$

is the Green's function for the three-dimensional Helmholtz equation. In our simulations, we assume that the relative permittivity of the host medium is 4.8, as it is commonly used in experimental setups [3].

In (4), $\boldsymbol{E^i}(\boldsymbol{r})$ is the incident electric field, which depends on the kind of the source to excite the MM structure. For example, we model small antennas by using Hertzian dipole represented by

$$\boldsymbol{E^i}(\boldsymbol{r}) = ik\eta\frac{\exp(iks)}{4\pi s}\left\{\bar{\mathbf{I}}_{DM}\left[1+\frac{i}{ks}-\frac{1}{k^2s^2}\right]-\bar{\mathbf{I}}_{DM}\cdot\hat{\boldsymbol{s}}\hat{\boldsymbol{s}}\left[1+\frac{3i}{ks}-\frac{3}{k^2s^2}\right]\right\}, \tag{6}$$

where $\bar{\mathbf{I}}_{DM}$ is the dipole moment,

$$s = \sqrt{(\boldsymbol{r}-\boldsymbol{r}_0)\cdot(\boldsymbol{r}-\boldsymbol{r}_0)}, \qquad \hat{\boldsymbol{s}} = \frac{\boldsymbol{r}-\boldsymbol{r}_0}{s}, \tag{7}$$

and $\boldsymbol{r}_0$ is the location of the dipole. To model the antennas with focussed radiations involving a main beam, we employ the complex-source-point approach by taking $\boldsymbol{r}_0$ as a vector with complex coordinates in (6) and (7). Finally, we also simulate dipole antennas with different lengths using a delta-gap source defined at the center of a strip located near the MM structure.

The dense matrix equation in (2) is solved iteratively using a Krylov subspace method such as stabilized biconjugate gradient algorithm. In addition, due to the large numbers of unknowns, matrix-vector multiplications are accelerated by MLFMA running on a single computer or on a parallel cluster of computers. In MLFMA, only the near-field interactions are calculated directly by evaluating the double integration in (3), but the rest are calculated in group-by-group manner as [2]

$$Z^E_{mn} = \left(\frac{ik}{4\pi}\right)^2\int d^2\hat{\boldsymbol{k}}\boldsymbol{F}^{rec}_{Cm}(\boldsymbol{k})T_L(\boldsymbol{k},\boldsymbol{D})\cdot\boldsymbol{F}^{rad}_{C'n}(\boldsymbol{k}), \tag{8}$$

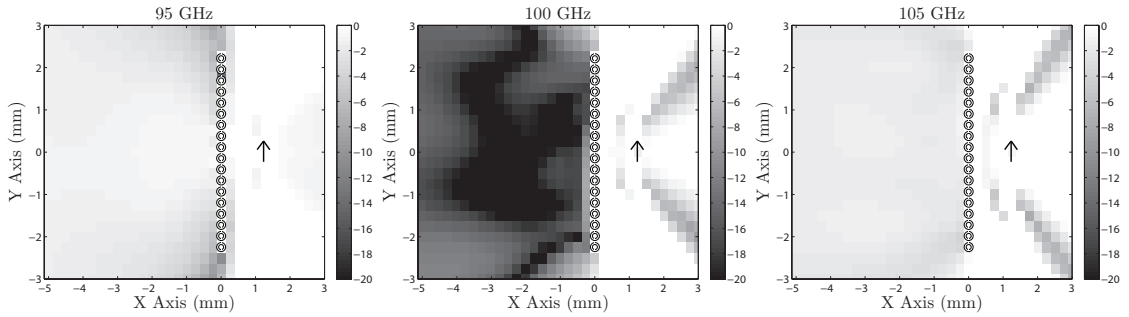

Fig. 3. Power transmission for the 1-layer SRR array depicted in Fig. 1(b) at 95 GHz, 100 GHz, and 105 GHz. SRRs and the ideal (Hertzian) dipole are also depicted in the figures and the transmission region is on the left of the array.

where

$$T_L(\boldsymbol{k}, \boldsymbol{D}) = \sum_{l=0}^{L} i^l (2l+1) h_l^{(1)}(kD) P_l(\hat{\boldsymbol{D}} \cdot \hat{\boldsymbol{k}}) \tag{9}$$

is the translation function written in terms of the spherical Hankel function of the first kind $h_l^{(1)}$ and Legendre polynomial P_l. In (8), $\boldsymbol{F}_{Cm}^{rec}$ and $\boldsymbol{F}_{C'n}^{rad}$ are the receiving and radiation patterns of the mth testing function and nth basis function, respectively. The radiation pattern $\boldsymbol{F}_{C'n}^{rad}$ with respect to C' is translated by $T_L(\boldsymbol{k}, \boldsymbol{D})$ into an incoming wave at point C located at $\boldsymbol{r}_C = \boldsymbol{r}_{C'} + \boldsymbol{D}$. Then, the incoming wave is received by the mth testing function that has the receiving pattern $\boldsymbol{F}_{Cm}^{rec}$ with respect to a close point C.

MLFMA employs the diagonalization in (8) to calculate the interactions between the basis and testing groups. In the multilevel clustering scheme, the MM structure is included in a computational volume, which is recursively divided into sub-volumes. Then a tree structure formed, on which the MLFMA steps are performed, such as aggregation, translation, and disaggregation. This way, the computational complexity and the memory requirement for a matrix-vector multiplication is reduced from $O(N^2)$ to $O(N \log N)$. MLFMA is detailed in [2].

EFIE usually produces ill-conditioned matrix equations that are difficult to solve by an iterative algorithm [4]. In addition, MM structures usually present numerical resonances, which further inhibits a quick convergence without preconditioning. To obtain a convergence in a reasonable number of iterations, we employ near-field preconditioner (NFP) obtained by retaining all of the available near-field interactions. NFP is not commonly used in the solutions of large scattering problems, since it has a complexity larger than MLFMA. However, for all problems investigated in this work, we observe that the additional time required for the factorization and use of NFP is smaller than the time gained by the reduction of the iterations.

3. Results

Fig. 2 presents the results for the 1-layer TW array in Fig. 1(a), where the power transmission is plotted at various frequencies, i.e., 95 GHz, 100 GHz, and 110 GHz. The transmission is calculated at different points in the $z = 0$ plane and the TW array is depicted in the plots. The excitation is a Hertzian dipole oriented in the y direction as also indicated in the plots

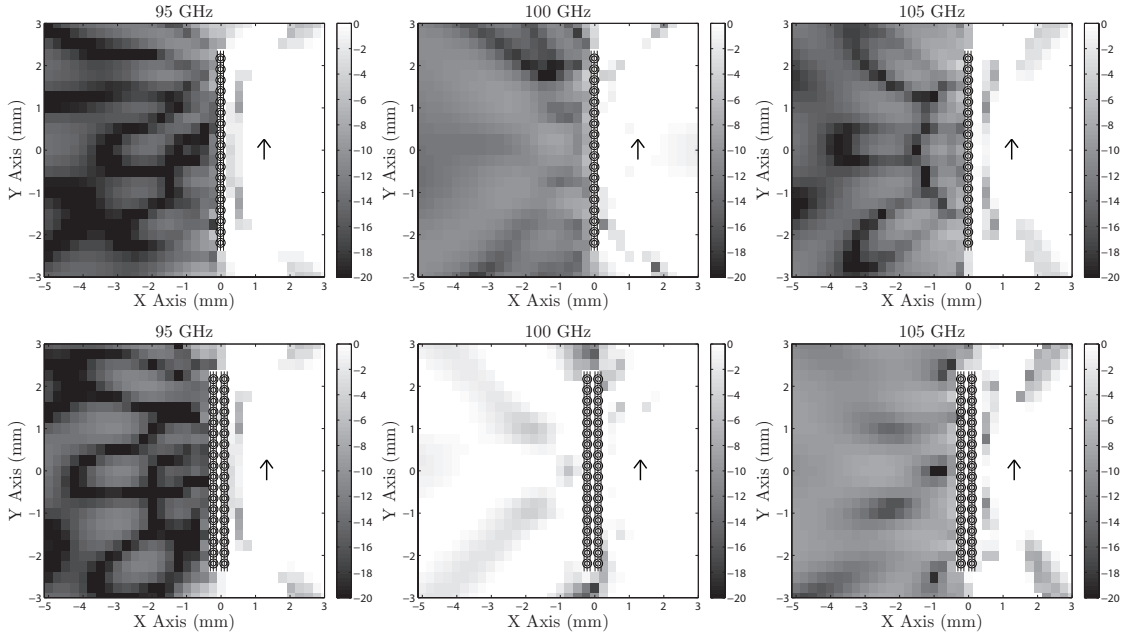

Fig. 4. Power transmission for the 1-layer and 2-layer CMM arrays depicted at 95 GHz, 100 GHz, and 105 GHz. The arrays and the ideal (Hertzian) dipole are also depicted in the figures and the transmission region is on the left of the arrays.

and the transmission region is on the left of the TW array. Fig. 2 shows that the TW array prevents the fields from passing into the transmission region at all three frequencies. Next, Fig. 3 presents the response of the SRR array in Fig. 1(b) at the same frequencies. At 95 GHz and 105 GHz, the power transmission through the SRR array is almost unity, which corresponds to 0 decibels (dB). On the other hand, around the resonance frequency (100 GHz), the transmitted power drops dramatically due to the shadowing effect of the SRR array. In other words, negative effective permeability is stimulated in the medium at 100 GHz.

Fig. 4 presents the power transmission for the 1-layer and 2-layer CMM arrays constructed by employing the SRR and TW arrays in Fig. 1. At 95 GHz and 105 GHz, we observe that the array blocks the fields and this is mainly due to the negative effective permittivity introduced by the TWs. On the other hand, the transmission through the CMM array increases at 100 GHz, which is more visible in the 2-layer case. The reason is that the SRRs resonate around 100 GHz as depicted in Fig. 3. Then, both the effective permittivity and permeability stimulated in the medium become negative. This is also visible in Fig. 5, where the power transmission at $(x, y) =$ (-1.25 mm, 0 mm) is plotted with respect to frequency for 1-layer and 2-layer SRR, TW, and CMM arrays. Around 100 GHz, the transmission through the CMM array increases, even above 0 dB for the 2-layer case. We note that increasing the number of layers extends the frequency range for the low and high transmissions through the SRR and CMM arrays, respectively.

Finally, the number of iterations for the solutions of SRR, TW, and CMM problems are depicted in Fig. 6 with respect to frequency. These iterations are obtained when NFP is employed, which includes all the available interactions of MLFMA. We observe that there exists a numerical resonance at 95 GHz for the SRR and CMM arrays so that the number of

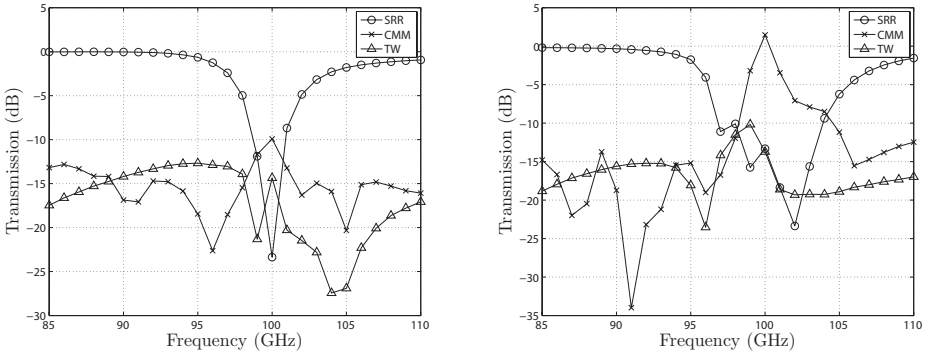

Fig. 5. Power transmission at (x, y) = (-1.25 mm, 0 mm) for the (a) 1-layer and (b) 2-layer SRR, TW, and CMM arrays with respect to frequency.

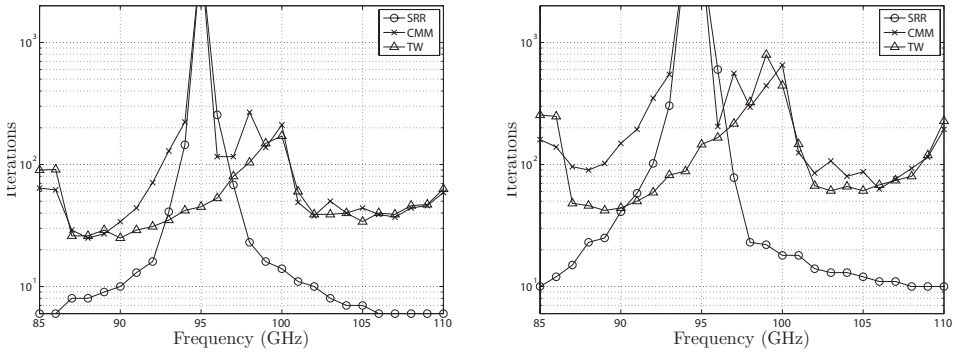

Fig. 6. Iteration counts for the solutions of (a) 1-layer and (b) 2-layer SRR, TW, and CMM arrays with respect to frequency.

iterations exceeds 2000. It is remarkable that the numerical resonance is different from the physical resonance of SRRs, which is at 100 GHz. To obtain a convergence at these special frequencies, we reduce the number of levels of MLFMA and enrich the near-field matrix. For larger arrays with more layers, this strategy may fail to provide a solution with the existing computational resources. Then, we employ stronger and more efficient preconditioners based on advanced techniques, such as two-level preconditioning.

References

[1] S. M. Rao, D. R. Wilton, and A. W. Glisson, "Electromagnetic scattering by surfaces of arbitrary shape," *IEEE Trans. Antennas Propagat.*, vol. AP-30, pp. 409–418, May 1982.

[2] W. C. Chew, J.-M. Jin, E. Michielssen, and J. Song, *Fast and Efficient Algorithms in Computational Electromagnetics*. Boston, MA: Artech House, 2001.

[3] M. Gokkavas, K. Güven, I. Bulu, K. Aydın, R. S. Penciu, M. Kafesaki, C. M. Soukoulis, and E. Özbay, "Experimental demonstration of a left-handed metamaterial operating at 100 GHz," *Phys. Rev. B.*, vol. 73, no. 193103, 2006.

[4] L. Gürel and Ö. Ergül, "Comparisons of FMM implementations employing different formulations and iterative solvers," *2003 IEEE AP-S International Symposium*, Columbus, Ohio, vol. 1, pp. 19–22, June 2003.